Multi-time scale identification of key kinetic processes for lithium-ion batteries considering variable characteristic frequency.

SHI, H., WANG, S., LIANG, J., TAKYI-ANINAKWA, P., YANG, X., FERNANDEZ, C. and WANG, L.

2023

Multi-time scale identification of key kinetic processes for lithium-ion batteries considering variable characteristic frequency

Haotian Shi[a], Shunli Wang[a,*], Jianhong Liang[b], Paul Takyi-Aninakwa[a], Xiao Yang[a], Carlos Fernandez[c], Liping Wang[b,*]

[a]*School of Information Engineering, Southwest University of Science and Technology, Mianyang 621010, Sichuan, China*
[b]*Department of Mechanical Engineering, Tsinghua University, Beijing 100084, China*
[c]*School of Pharmacy and Life Sciences, Robert Gordon University, Aberdeen AB10-7GJ, UK*

*Corresponding authors.
E-mail addresses: wangshunli@swust.edu.cn (S.L. Wang); lpwang@mail.tsinghua.edu.cn (L.P. Wang).

Abstract: The electrification of vehicles puts forward higher requirements for the power management efficiency of integrated battery management systems as the primary or sole energy supply. In this paper, an efficient adaptive multi-time scale identification strategy is proposed to achieve high-fidelity modeling of complex kinetic processes inside the battery. More specifically, a second-order equivalent circuit model network considering variable characteristic frequency is constructed based on the high-frequency, medium-high-frequency, and low-frequency characteristics of the key kinetic processes. Then, two coupled sub-filters are developed based on forgetting factor recursive least squares and extended Kalman filtering methods and decoupled by the corresponding time-scale information. The coupled iterative calculation of the two sub-filter modules at different time scales is realized by the voltage response of the kinetic diffusion process. In addition, the driver of the low-frequency subalgorithm with the state of charge variation amount as the kernel is designed to realize the adaptive identification of the kinetic diffusion process parameters. Finally, the concept of dynamical parameter entropy is introduced and advocated to verify the physical meaning of the kinetic parameters. The experimental results under three operating conditions show that the mean absolute error and root-mean-square error metrics of the proposed strategy for voltage tracking can be limited to 13 and 16 mV,

respectively. Additionally, from the entropy calculation results, the proposed method can reduce the dispersion of parameter identification results by a maximum of 40.72% and 70.05%, respectively, compared with the traditional fixed characteristic frequency algorithms. The proposed method paves the way for the subsequent development of adaptive state estimators and efficient embedded applications.

Keywords: Lithium-ion battery; Kinetic parameters; Entropy evaluation; Parameter identification; Frequency characteristic

1 Introduction

As a part of the global decarburization efforts, it is crucial for the electrification and intellectualization of internal combustion engine-powered vehicles [1,2]. Among various types of electrified vehicles, compared with plug-in hybrid electric vehicles (PHEVs), hybrid electric vehicles (HEVs), and fuel cell electric vehicles (FCEVs) with the battery-motor system as the main energy source [3–5], the development prospect of battery electric vehicles (BEVs) as the only power source seems to be widely optimistic under the current decarbonization agenda [6,7]. In view of the requirements of the battery energy system, lithium-ion batteries are favored due to their unique properties, such as high energy density (>200 Wh/kg [8]), high working voltage (>3.0 V [9]), and long cycle life (>1000 cycles [10]), compared with lead-acid batteries and other oxide batteries [11]. The battery energy systems integrate electrochemistry, thermodynamics, and mechanics, making them highly nonlinear [12,13]. Therefore, it is very critical to develop an efficient management strategy to ensure the safe, reliable, and long-term use of lithium-ion batteries.

As the core of the whole battery management system (BMS) development, the upper application algorithm for monitoring the internal states, such as state of charge (SOC), state of power (SOP), and

state of health (SOH) of the battery, is very significant [14,15]. In many types of research and applications, the algorithms for internal state monitoring are designed based on the battery model [12,16]. This leads to the undeniable conclusion that the performance of condition-monitoring algorithms is highly dependent on the accuracy of the battery modeling [17]. Since the kinetic processes inside the battery exhibit some differences in time scales. In this case, battery modeling considering multi-time scale information could further improve the fidelity of the model, thus paving the way for the development of effective management strategy. In addition, an efficient BMS should balance the dual requirements of modeling accuracy and computational complexity, which in turn provides guarantees for embedded system applications.

The high-fidelity model and accurate internal characterization can greatly improve the management efficiency of batteries and prolong their life. In the modeling of power batteries, the widely used electrochemical mechanism model (EMM) and equivalent circuit model (ECM) have obvious advantages in development potential compared with other battery models. Previous studies have shown that the EMM and ECM of power batteries have different application scenarios in engineering applications [18,19]. With the modeling idea dominated by the electrochemical reaction principle, the EMM is usually used to design and optimize the battery [18,20]. More specifically, the EMMs have obvious advantages in capturing external macro physical quantities (such as current, voltage, etc.) and internal key characteristic parameters (such as the conduction rate of carriers in the solid-liquid phase and the time constant of chemical reactions, etc.) [21]. However, the EMM contains too many parameters that are challenging to identify due to the partial differential equations [22]. As a result, the lightweight requirements of embedded applications may not be satisfied by the system identification methods developed based on the EMM. Furthermore, the convergence, stability, and speed of highly

computationally complex algorithms cannot be efficiently guaranteed during the system's iterative update.

On the other hand, the ECM developed based on mature circuit theory is widely used in the real-time control of the BMS because of its high computational efficiency and generally satisfactory accuracy [23–26]. However, a non-negligible shortcoming is that the ECM is relatively weak in characterizing the internal complex battery kinetic behavior. One of the primary reasons is that the battery's internal dynamic processes have significant frequency differences and multi-time time scale characteristics. The battery modeling that ignores the multi-time scale information of kinetic processes may reduce the accuracy of kinetic parameter identification. In this case, extracting and analyzing the time-scale information inside the battery and using it for the optimization of ECMs is an effective way for high-fidelity modeling. In addition to EMM and ECM, battery modeling designs based on data-driven or artificial intelligence algorithms have been widely carried out and show obvious potential advantages in the networked, intelligent, and cloud-based collaboration of EVs [27,28]. Nevertheless, with the current hardware and on-board chip requirements, these methods do not seem to be directly implantable for use in engineering.

Considering the variable characteristic frequency of key kinetic processes inside the cell is extremely crucial to improve the accuracy and fidelity of the battery model. Among the key kinetic processes within the battery, such as ion migration, charge transfer and active lithium diffusion, can be monitored in a non-destructive manner and exhibit certain time-scale differences [29–32]. This provides a good opportunity to distinguish and quantify the kinetic processes inside the battery. In this case, extracting and analyzing time scale information from key dynamics is extremely beneficial in improving the accuracy of the battery model [33,34]. For the key dynamic processes inside the battery, such as the

charge transfer process, electric double layer process, and diffusion process, the time scale difference can be described as having four main characteristics [35,36]. First, the physical process at high-frequency is that lithium ions mainly pass through the separator, and electrons pass through the current collector and external circuit. Secondly, the physical process at a medium-high frequency can be described as the migration of lithium ions to the liquid phase and the chemical reaction of active lithium at the solid-liquid interface. Thirdly, the diffusion of active lithium in solid particles is characterized by low-frequency. Finally, the increase of polarization resistance and capacitance in the electrode is characterized by ultra-high frequency. The variable characteristic frequency of the kinetic process brings a great challenge to the high-fidelity modeling of the battery.

In addition to constructing high-fidelity battery models, the development of lightweight parameter identification strategies is highly significant in engineering applications. The multi-time scale problem of the kinetic process has an impact on the design of the model parameter identification algorithm. In most of the current research, the recursive least squares (RLS) algorithm [37–41] and other adaptive filtering methods [42–44], such as the extended Kalman filter (EKF) [45,46], are widely used in engineering applications due to their moderate appropriate computational complexities. However, ignoring the identification strategy of dynamic time scale information may weaken the physical meaning of model parameter identification results. Moreover, it is an unreasonable phenomenon that the modeled values of terminal voltages can be satisfied with a good matching effect with the measured values even though the model parameters are identified inaccurately. Therefore, it is extremely essential to develop an efficient online adaptive identification algorithm to realize accurate identification of dynamic processes.

To solve this problem, an efficient adaptive multi-time scale identification strategy based on

second-order resistance-capacitance (RC) ECM network considering variable characteristic frequency is proposed in this paper. The four main contributions make this research different from existing ones.

(1) Considering the dual index requirements of computational complexity and model accuracy, the second-order RC ECM network based on the variable characteristic frequency is established to realize the capture of key kinetic processes inside the battery.

(2) To make the identification results of kinetic parameters have clear physical significance, an efficient adaptive multi-time scale identification strategy is developed in detail. The iterative identification of key kinetic parameters is realized at different time scales.

(3) The variation in SOC levels is used to design the driver that controls the low-frequency sub-filter to improve the adaptability and generality of the proposed strategy. The sub-filters in different frequency bands are strongly coupled by diffusion voltage and decoupled by time-scale information.

(4) The concept of parameter entropy is introduced and advocated. Furthermore, the entropy value is calculated under three different current conditions to verify the rationality of the parameter identification results and the superiority of the proposed method.

The remainder of this paper is organized as follows: the battery model framework considering variable characteristic frequency is introduced in Section 2. The development of the proposed adaptive multi-time scale identification strategy is given in Section 3. Experimental verification and discussions are described in Section 4. The conclusions are finally drawn in Section 5.

2 Model framework considering variable characteristic frequency

2.1 Second-order RC circuit network model

Charge transfer and diffusion are two of the most important effects in battery dynamics, which are

usually described by two different RC circuits in the ECM. In this paper, the second-order RC ECM is still used to capture the variable characteristic frequency of the battery. The corresponding relationship between the kinetic process and the frequency characteristics is shown in Fig. 1(a and b). Affected by the variable characteristic frequency of the kinetic processes inside the battery, the use of traditional fixed characteristic frequency identification algorithms to directly identify all the characteristic parameters inevitably produces inaccurate results and even lead to unreliable results under adverse operating conditions.

Based on the fact that the second-order RC ECM can accurately simulate the key kinetic processes in the battery, this paper proposes an efficient adaptive multi-time scale identification strategy based on frequency feature separation to improve the effectiveness of model parameters. In this strategy, the medium-high-frequency RC network is composed of a transfer charge resistor and an electric double-layer capacitor. Also, the low-frequency RC network composed of a diffusion resistor and a diffusion capacitor is designed separately in different filter modules. The idea of the characteristic separation modeling strategy based on second-order RC ECM development is shown in Fig. 1(c).

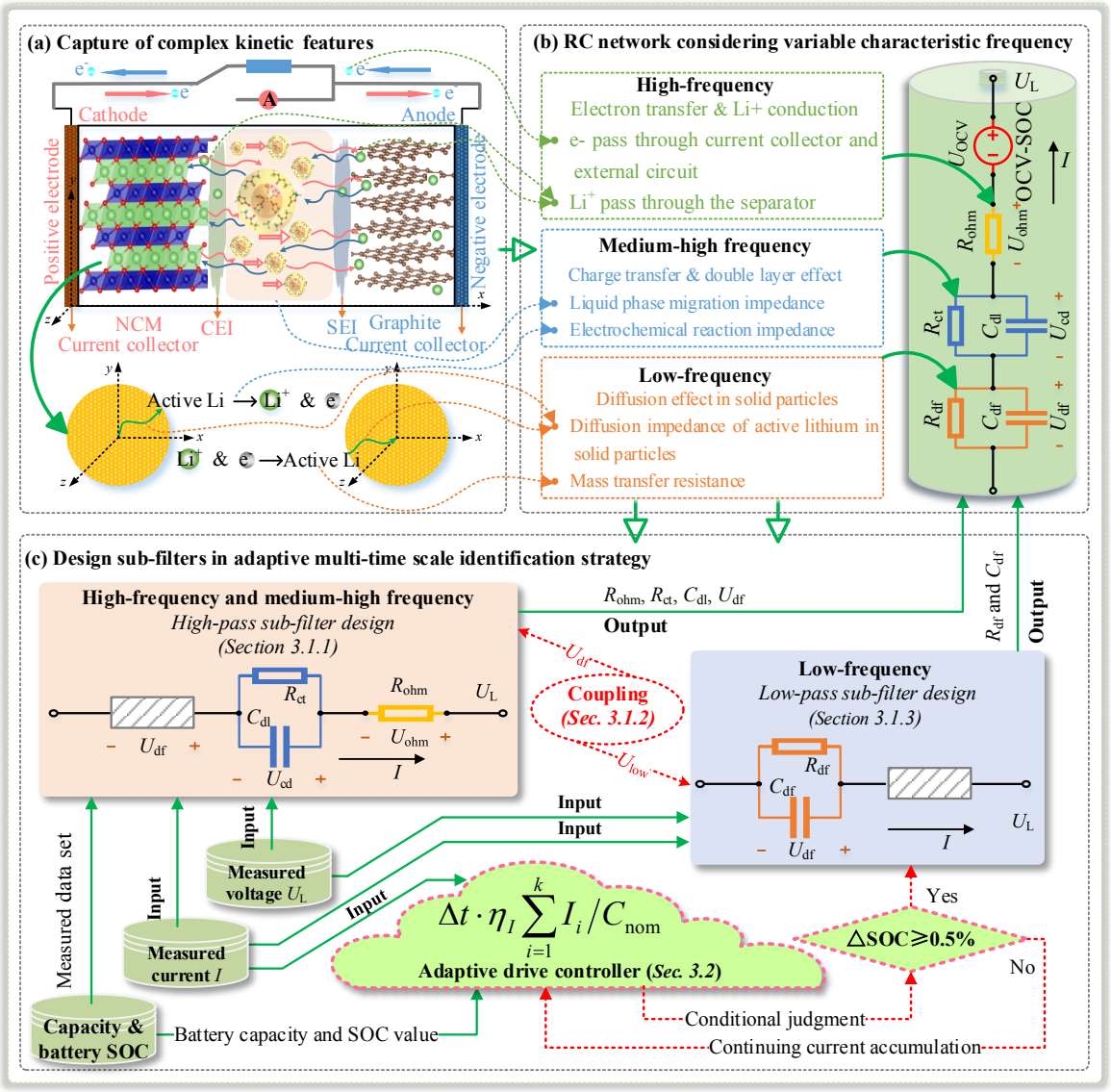

Fig. 1. Architecture for modeling based on second-order RC ECM. (a) The capture of complex kinetic features; (b) a second-order RC ECM considering variable characteristic frequency; (c) modeling strategies for the separation of key kinetic processes.

In Fig. 1(a and b), the resistance of internal carrier conduction in lithium-ion batteries can correspond to the impedance link in the second-order RC ECM. Specifically, the nonlinear open-circuit voltage (OCV) of the battery is characterized by U_{OCV}, and its calculation method is calculated from the prior data of OCV-SOC; U_{L} is the closed-circuit terminal voltage of the second-order RC ECM; I denotes the current excitation of the system. In this paper, the battery discharging is assumed to be in the

positive direction. On the extraction and analysis of key kinetic processes inside the battery, the high-frequency characteristic is described as ohmic resistance, which is recorded as R_{ohm}, and the voltage drop at both ends is recorded as U_{ohm}. The medium-high frequency characteristics are described as charge transfer and double-layer impedance, which are recorded as R_{ct} and C_{dl}, and the voltage drop at both ends is recorded as U_{cd}. The low-frequency characteristic is described as diffusion impedance, which is recorded as R_{df} and C_{df}, and the voltage drop at both ends is recorded as U_{df}. It is worth noting that the current excitation at ultra-high frequency rarely appears in actual EV driving conditions. Therefore, the inductance effect at an ultra-high frequency can be ignored, which is suitable for the practical application of vehicle EV battery systems and avoids the modeling error caused by nonlinear inductance.

In addition, it can be observed from Fig. 1(c) that the medium-high frequency parameters and the low-frequency parameters are divided into two different modules. Each module is controlled by an independent filtering algorithm. It is worth noting that we allocate the internal ohmic resistance at a high frequency and the transfer charge impedance at a medium-high frequency in the same module. There are two main reasons for this distribution. Firstly, the reaction time of ohmic resistance in the medium-high frequency band is in milliseconds to the second level. The reaction time of impedance parameters in the medium-high frequency band is in the second level. The time constants of the two to complete their respective physical processes have a certain coincidence in the second level. Secondly, in the current vehicle-mounted BMS, the sampling frequency of the electronic control unit (ECU) can be controlled. Therefore, the data saturation phenomenon of medium-high frequency parameter identification caused by too high a sampling frequency will not occur.

2.2 Model-based modular state representation

The terminal voltages of the second-order RC ECM mainly include ohmic impedance voltage U_{ohm}, charge transfer, and electric double-layer impedance voltage U_{cd}, diffusion impedance voltage U_{df}, and open-circuit voltage U_{OCV}. Assuming that the sampling period Δt remains constant during the system operation, the full-response equations of U_{cd} and U_{df} at time step k can be obtained based on the steady-state analysis of the RC network in circuit theory, as shown in Eqs. (1) and (2).

$$U_{\mathrm{cd},k} = \exp\left(-\Delta t/R_{\mathrm{ct}}C_{\mathrm{dl}}\right)U_{\mathrm{cd},k-1} + R_{\mathrm{ct}}\left(1-\exp\left(-\Delta t/R_{\mathrm{ct}}C_{\mathrm{dl}}\right)\right)I_{k-1} \tag{1}$$

$$U_{\mathrm{df},k} = \exp\left(-\Delta t/R_{\mathrm{df}}C_{\mathrm{df}}\right)U_{\mathrm{df},k-1} + R_{\mathrm{df}}\left(1-\exp\left(-\Delta t/R_{\mathrm{df}}C_{\mathrm{df}}\right)\right)I_{k-1} \tag{2}$$

where k represents the sampling point of the BMS, and Δt represents the sampling interval of the measured current and measured voltage. I_{k-1} is the system input current at the time step k−1, $U_{\mathrm{cd},k}$ and $U_{\mathrm{df},k}$ are the terminal voltages of the corresponding resistor-capacitor network at the time step k, respectively. Then, the overall terminal voltage of the second-order RC ECM can be calculated using Eq. (3).

$$U_{\mathrm{L},k} = U_{\mathrm{OCV},k} + U_{\mathrm{ohm},k} + U_{\mathrm{cd},k} + U_{\mathrm{df},k} \tag{3}$$

In addition, the SOC is defined as a percentage of the battery's remaining capacity compared to the nominal capacity of the battery in many Refs. [4,47]. When the nominal capacity of the battery and the initial SOC value is obtained, the reference SOC is calculated using the Coulomb counting method based on high confidence under laboratory conditions. The mathematical expression for its calculation is shown in Eq. (4).

$$z_k = z_0 + \Delta t \cdot \eta_I \sum_{i=1}^{k} I_i / C_{\mathrm{nom}} \tag{4}$$

where C_{nom} indicates the available nominal capacity, η_I represents the Coulombic efficiency factor, z represents the SOC of the battery for brevity, z_0 and z_k represent the SOC values at time step 0

and k, respectively. It should be noted that a small capacity battery of model 18650 with 2.0 A h is chosen as the sample cell for the experiments in this paper, so the value of η_I is 1. In addition, since the current state of the battery is known and the experimental conditions are controllable, the effects of many indicators, such as cell aging state, current multiplication rate, and ambient temperature on capacity, are neglected.

2.3 Entropy definition of model parameters

Entropy is often used to describe the chaotic degree of a system. The more chaotic the energy distribution, the greater the entropy [48–50]. In this paper, the concept of entropy is ingeniously introduced into battery modeling to enrich the performance verification of the model. The correlation is that the smaller the entropy value, the more obvious the physical meaning of the parameters, the higher the consistency of the parameter identification results, and the better the reliability. Under this concept, the definition of entropy can be simply calculated using Eq. (5).

$$\mathrm{En}_y^x = \frac{\left|\bar{y}^x - \tilde{y}\right|}{\tilde{y}} \times 100\% \tag{5}$$

where En_y^x represents the symbolic expression of the entropy value of internal ohmic resistance, expressed as a percentage, indicating the degree to which internal ohmic resistance deviates from the average value using different algorithms. x denotes different recognition methods, y denotes the dynamical parameters in the model. In this paper, x represents forgetting factor recursive least squares (FFRLS), EKF, and the proposed adaptive multi-time scale identification strategy. y can represent R_{ohm}, R_{ct}, C_{dl}, R_{df}, and C_{df}. $\bar{y}^x$ is the average value of the dynamical parameters identification results based on algorithm x in the whole sequence. $\tilde{y}$ is the average of the $\bar{y}^x$ obtained under different identification methods, and the mathematical expression for its calculation is shown in Eq. (6).

$$\tilde{y} = \frac{1}{n}\sum_{1}^{n}\bar{y}_n^x \tag{6}$$

where n is the number of adopted methods. Eqs. (5) and (6) show that after we obtain the model parameter identification results using different methods, $\bar{y}^x$ is obtained using each method, and the values of $\tilde{y}$ and En_y^x are further calculated. Similarly, the entropy of other impedance parameters in the model can be calculated by the same method. It is worth noting that when n is 1, $\bar{y}^x$ is equal to $\tilde{y}$ due to insufficient comparison of results. At this point, the entropy of all parameters is 0. In this case, the effectiveness of entropy can generally be reflected at least when two or more algorithms are compared. In this paper, FFRLS and EKF are selected to compare the performance of the proposed adaptive multi-time scale identification strategy, so the value of n is 3.

3 Adaptive multi-time scale identification strategy

In the modeling idea considering variable characteristic frequency, sub-algorithms at different frequencies are expected to identify key kinetic processes with different characteristics. In each cycle of the BMS, the input current and voltage of the system are used to identify the medium-high frequency characteristic parameters. But the diffusion impedance parameters with low-frequency characteristics do not need to be identified in every sampling period of the BMS. In other words, the same system input current and voltage parameters cannot be directly used to drive the operation of the low-frequency sub-filter. For this reason, this paper designs an adaptive drive controller for low-frequency sub-filter start-stop based on the current profile. It is obvious that with this separation identification strategy, considering the characteristics of the frequency difference, the identification results of the model parameters show a distinct physical meaning while ensuring high accuracy.

3.1 Model-based sub-algorithm development

3.1.1 Sub-algorithm design for medium-high frequency

According to this modeling concept, two separate high-pass and low-pass filters must be developed to capture impedance parameters at various frequencies and improve the model's ability to simulate real-world battery dynamics. Naturally, an important problem needs to be solved, namely, the sub-algorithm design of filters at different frequencies. In this paper, for the sub-algorithm design in the medium-high-frequency band filters, the FFRLS is implementation, and the effectiveness of this method is verified in Refs. [51,52].

Considering the requirements of the FFRLS algorithm, it is necessary to derive the exogenous autoregressive equation of input and output. In view of this, we define the voltage inside the battery to overcome the electrochemical reaction process as U_P, which is obtained as

$$U_{p,k} = U_{\mathrm{L},k} - U_{\mathrm{OCV},k} = I_k R_{\mathrm{ohm},k} + U_{\mathrm{cd},k} + U_{\mathrm{df},k} \tag{7}$$

Then, the frequency domain form of the corresponding loop equation in the medium-high frequency band is obtained by the Laplace transform, as shown in Eq. (8).

$$G(s) = U_p(s) / I(s) = R_{\mathrm{ohm}} + R_{\mathrm{ct}} / \left(1 + R_{\mathrm{ct}} C_{\mathrm{dl}} s\right) + U_{\mathrm{df}}(s) \tag{8}$$

where s is the Laplace operator, and $G(s)$ is the transfer function of the impedance network. Further, the difference equation of the whole impedance link can be obtained, as shown in Eq. (9).

$$U_{p,k} = \kappa_1 U_{p,k-1} + \kappa_2 I_k + \kappa_3 I_{k-1} + \kappa_4 \tag{9}$$

where κ_1, κ_2, κ_3, and κ_4 are the coefficients of the difference equation, the expanded form is shown in Eqs. (10)–(13).

$$\kappa_1 = R_{\mathrm{ct}} C_{\mathrm{dl}} / \left(\Delta t + R_{\mathrm{ct}} C_{\mathrm{dl}}\right) \tag{10}$$

$$\kappa_2 = \left(\left(R_{\mathrm{ohm}} + R_{\mathrm{ct}}\right)\Delta t + R_{\mathrm{ohm}} R_{\mathrm{ct}} C_{\mathrm{dl}}\right) / \left(\Delta t + R_{\mathrm{ct}} C_{\mathrm{dl}}\right) \tag{11}$$

$$\kappa_3 = R_{\mathrm{ohm}} R_{\mathrm{ct}} C_{\mathrm{dl}} / \left(\Delta t + R_{\mathrm{ct}} C_{\mathrm{dl}}\right) \tag{12}$$

$$\kappa_4 = \left(\left(\Delta t + R_{\mathrm{ct}} C_{\mathrm{dl}}\right) U_{\mathrm{df},k} - R_{\mathrm{ct}} C_{\mathrm{dl}} U_{\mathrm{df},k-1}\right) / \left(\Delta t + R_{\mathrm{ct}} C_{\mathrm{dl}}\right) \tag{13}$$

From Eqs. (10)–(13), k and Δt represent the sampling point of BMS and the sampling interval of current and voltage, respectively. Furthermore, the exogenous autoregressive equation used for the iteration of the FFRLS algorithm can be defined, as shown in Eq. (14).

$$\boldsymbol{Y}_{\mathrm{high},k} = \boldsymbol{\theta}_{\mathrm{high},k} \boldsymbol{H}^{\mathrm{T}}_{\mathrm{high},k} \tag{14}$$

where $\boldsymbol{Y}_{\mathrm{high},k}$, $\boldsymbol{\theta}_{\mathrm{high},k}$, and $\boldsymbol{H}_{\mathrm{high},k}$ are the output matrix, coefficient matrix, and system input matrix of the difference equation in the medium-high frequency band, respectively. The expansion forms of each matrix are as follows:

$$\boldsymbol{Y}_{\mathrm{high},k} = [U_{p,k}] \tag{15}$$

$$\boldsymbol{H}_{\mathrm{high},k} = [U_{P,k-1} \quad I_k \quad I_{k-1} \quad 1] \tag{16}$$

$$\boldsymbol{\theta}_{\mathrm{high},k} = [\kappa_{1,k} \quad \kappa_{2,k} \quad \kappa_{3,k} \quad \kappa_{4,k}] \tag{17}$$

Then, the identification of the coefficient matrix $\boldsymbol{\theta}_{\mathrm{high},k}$ at each time step can be obtained based on the recursion of the FFRLS algorithm. The specific recursive equation is as follows:

At the time $k = 0$, initialization:

$$\hat{\boldsymbol{\theta}}_{\mathrm{high},0} = E[\boldsymbol{\theta}_{\mathrm{high},0}] \tag{18}$$

$$\boldsymbol{P}_{\mathrm{high},0} = [(\hat{\boldsymbol{\theta}}_{\mathrm{high},0} - \boldsymbol{\theta}_{\mathrm{high},0})(\hat{\boldsymbol{\theta}}_{\mathrm{high},0} - \boldsymbol{\theta}_{\mathrm{high},0})^{\mathrm{T}}] \tag{19}$$

At the time $k = 1, 2, \ldots$, repeat:

$$K_{\mathrm{high},k} = (\boldsymbol{P}_{\mathrm{high},k-1} \boldsymbol{H}_{\mathrm{high},k}) / (\lambda + \boldsymbol{H}^{\mathrm{T}}_{\mathrm{high},k} \boldsymbol{P}_{\mathrm{high},k-1} \boldsymbol{H}_{\mathrm{high},k}) \tag{20}$$

$$\boldsymbol{P}_{\mathrm{high},k} = \boldsymbol{P}_{\mathrm{high},k-1} - K_{\mathrm{high},k} \boldsymbol{H}^{\mathrm{T}}_{\mathrm{high},k} \boldsymbol{P}_{\mathrm{high},k-1} / \lambda \tag{21}$$

$$\hat{\boldsymbol{\theta}}_{\mathrm{high},k} = \hat{\boldsymbol{\theta}}_{\mathrm{high},k-1} + K_{\mathrm{high},k} \left(\boldsymbol{Y}_{\mathrm{high},k} - \hat{\boldsymbol{\theta}}_{\mathrm{high},k-1} \boldsymbol{H}^{\mathrm{T}}_{\mathrm{high},k}\right) \tag{22}$$

From Eqs. (18)–(22), $K_{\text{high},k}$ and $P_{\text{high},k}$ are the gain matrix and covariance matrix of the medium-high-frequency sub-algorithm at the time step k, respectively. $\hat{\boldsymbol{\theta}}_{\text{high},k}$ is the parameter matrix used to store the coefficient recursion results. Under the sampling data of the embedded BMS, each coefficient value in $\hat{\boldsymbol{\theta}}_{\text{high},k}$ can be recursively obtained using FFRLS algorithm. Further, the values of R_{ohm}, R_{ct}, and C_{dl} for the medium-high-frequency parameters can be calculated using Eqs. (10)–(12). Then, the low-frequency diffusion voltage U_{df} under each set of sampled data can be calculated through the results of R_{ohm}, R_{ct}, and C_{dl} in Eq. (13). It is worth noting that the calculation of U_{df} involves an iterative process, so its initialization is necessary during identification. In this paper, the U_{df} is initialized with 0, and the forgetting factor λ is set to 0.99. It is not difficult to find that after the FFRLS algorithm converges, the U_{df} identification results can also be considered to have high reliability.

3.1.2 Coupling factor between the sub-algorithms

As mentioned above, the adaptive multi-time scale identification strategy considering frequency characteristics distinguishes the medium-high frequency parameters from the low-frequency parameters in different filter modules. At this time, a crucial problem to be solved is how to choose the coupling factor between different sub-algorithms. It is worth noting that the sampling of the measured current and measured voltage has a high frequency in the BMS. In order not to contradict the kinetic information between medium-high frequency and low-frequency, the system measurement data cannot be directly applied in the low-frequency sub-algorithm. Moreover, the terminal voltage of the low-frequency impedance link cannot be directly measured. In this case, an effective feedback correction mechanism is urgently needed before the development of a low-frequency sub-algorithm.

It is also important to note that in engineering applications, the feedback correction mechanism of the adaptive filtering algorithm is often realized by the error between measurement and estimation.

Fortunately, while the identification results of medium-high-frequency parameters R_{ohm}, R_{ct}, and C_{dl} in the medium-high frequency filter module are obtained, an important physical quantity, namely the terminal voltage U_{df} of diffusion impedance, is also recursively calculated. The important point is that when the FFRLS algorithm converges, the identification result of U_{df} can be considered to have high reliability. Therefore, selecting U_{df} as the coupling factor between the two sub-filter modulessolves the problem of less effective innovation in the low-frequency impedance network. Under the effective feedback mechanism of U_{df}, the terminal voltage response of the low-frequency impedance link is defined as a function $g(*)$, as shown in Eq. (23).

$$g\left(U_{\mathrm{low},k}, I_k, R_{\mathrm{df},k}, C_{\mathrm{df},k}\right) = \exp\left(\frac{-\Delta t}{R_{\mathrm{df},k}C_{\mathrm{df},k}}\right)U_{\mathrm{low},k} + R_{\mathrm{df},k}\left(1-\exp\left(\frac{-\Delta t}{R_{\mathrm{df},k}C_{\mathrm{df},k}}\right)\right)I_k \tag{23}$$

where $U_{\mathrm{low},k}$ represents the low-frequency diffusion voltage at time step k. The function $g(*)$ indicates that the terminal voltage response of the low-frequency impedance link is influenced by the diffusion voltage $U_{\mathrm{low},k}$, current I_k, low-frequency diffusion resistance R_{df} and diffusion capacitance C_{df}. Then, the error innovation used for iterative correction of the algorithm in the low-frequency filter module can be calculated using Eq. (24).

$$\varepsilon_{\mathrm{low},k} = U_{\mathrm{df},m} - g\left(U_{\mathrm{low},k}, I_k, R_{\mathrm{df},k}, C_{\mathrm{df},k}\right) \tag{24}$$

where $\varepsilon_{\mathrm{low},k}$ is the coupling factor, which represents the error innovation of diffusion voltage in the low-frequency sub-algorithm. In addition, $U_{\mathrm{df},m}$ is the U_{df} identification result of the mth recursion under the medium-high-frequency sub-algorithm.

3.1.3 Sub-algorithm design for low-frequency

In the medium-high frequency sub-filter module designed based on the FFRLS algorithm, the identification results of parameters R_{ohm}, R_{ct}, C_{dl} and U_{df} can be obtained recursively. It should be

noted that the low-frequency impedance link corresponding to the slow diffusion of active lithium in solid particles can be regarded as a low-pass filter. That is to say, the terminal voltage response of low-frequency impedance can be regarded as the result of the long-term accumulation of current excitation. Based on this, we define the state variable of the low-frequency impedance link, as shown in Eq. (25).

$$\boldsymbol{\rho}_{\mathrm{low},k} = [R_{\mathrm{df},k} \quad C_{\mathrm{df},k}]^{\mathrm{T}} \tag{25}$$

where $\boldsymbol{\rho}_{\mathrm{low},k}$ is the state variable of the low-frequency sub-algorithm at time step k. Eqs. (23) and (25) are combined, and the state-space equation of the low-frequency impedance link in discrete form can be obtained, as shown in Eqs. (26) and (27).

$$\boldsymbol{\rho}_{\mathrm{low},k+1} = \boldsymbol{\rho}_{\mathrm{low},k} + \boldsymbol{w}_k \tag{26}$$

$$U_{\mathrm{low},k+1} = \exp\left(\frac{-\Delta t}{R_{\mathrm{df},k}C_{\mathrm{df},k}}\right)U_{\mathrm{low},k} + R_{\mathrm{df},k}\left(1-\exp\left(\frac{-\Delta t}{R_{\mathrm{df},k}C_{\mathrm{df},k}}\right)\right)I_k + v_k \tag{27}$$

Eq. (26) shows that the low-frequency impedance parameters are unchanged in nature, but are affected by some internal chemical reaction processes. Under this influence, the low-frequency impedance parameters will change slowly with the accumulation of time, and the process is realized by modeling with noise $\boldsymbol{w}_k$. Also, Eq. (27) shows that the low-frequency impedance link is realized by the sum of the full response and the estimation error v_k.

It is not difficult to find that the low-frequency diffusion voltage can be calculated by recursing using Eq. (27). However, once the values of low-frequency parameters R_{df} and C_{df} are not accurate enough, the low-frequency diffusion voltage U_{low} may deviate from its true value. This deviation from the true value error is inevitable due to the drawbacks of open-loop estimation. Note that the calculation of the coupling factor $\varepsilon_{\mathrm{low},k}$ includes the identification result of another U_{df} with high reliability, which provides enough effective information for the closed-loop correction of U_{df}. Under this idea, the EKF algorithm with low computational complexity is chosen to realize the development of a sub-

algorithm in a low-frequency filter module. In addition, the effectiveness of the EKF algorithm in system identification has been confirmed in many Refs. [12,34,40,41]. At this time, one of the main problems is to derive the system output matrix $C_{\mathrm{low},k}^{\rho}$ required for the EKF algorithm's iteration.

First, the following functions are defined by combining Eqs. (23) and (27).

$$g\left(U_{\mathrm{low},k}, I_k, \boldsymbol{\rho}_{\mathrm{low},k}\right)=\exp\left(\frac{-\Delta t}{R_{\mathrm{df},k}C_{\mathrm{df},k}}\right)U_{\mathrm{low},k}+R_{\mathrm{df},k}\left(1-\exp\left(\frac{-\Delta t}{R_{\mathrm{df},k}C_{\mathrm{df},k}}\right)\right)I_k \tag{28}$$

Then, the equation of the system output matrix $C_{\mathrm{low},k}^{\rho}$ can be obtained as follows:

$$C_{\mathrm{low},k}^{\rho}=\frac{\partial g(U_{\mathrm{low},k}, I_k, \boldsymbol{\rho}_{\mathrm{low},k})}{\partial \boldsymbol{\rho}_{\mathrm{low}}}=\frac{\partial g\left(U_{\mathrm{low},k}, I_k, \boldsymbol{\rho}_{\mathrm{low},k,}\right)}{\partial \boldsymbol{\rho}_{\mathrm{low}}}+\frac{\partial g\left(U_{\mathrm{low},k}, I_k, \boldsymbol{\rho}_{\mathrm{low},k}\right)}{\partial U_{\mathrm{low},k}}\frac{\mathrm{d}U_{\mathrm{low},k}}{\mathrm{d}\boldsymbol{\rho}_{\mathrm{low}}} \tag{29}$$

Further, each part of Eq. (29) is calculated as follows:

$$\frac{\partial g\left(U_{\mathrm{low},k}, I_k, \boldsymbol{\rho}_{\mathrm{low},k}\right)}{\partial \boldsymbol{\rho}_{\mathrm{low}}}=\left[\frac{\partial g\left(U_{\mathrm{low},k}, I_k, \boldsymbol{\rho}_{\mathrm{low},k}\right)}{\partial R_{\mathrm{df}}}\quad\frac{\partial g\left(U_{\mathrm{low},k}, I_k, \boldsymbol{\rho}_{\mathrm{low},k}\right)}{\partial C_{\mathrm{df}}}\right] \tag{30}$$

$$\frac{\partial g\left(U_{\mathrm{low},k}, I_k, \boldsymbol{\rho}_{\mathrm{low},k}\right)}{\partial R_{\mathrm{df}}}=\frac{\Delta t\left(U_{\mathrm{low},k}-R_{\mathrm{df},k}I_k\right)}{C_{\mathrm{df},k}\left(R_{\mathrm{df},k}\right)^2}\exp\left(\frac{-\Delta t}{R_{\mathrm{df},k}C_{\mathrm{df},k}}\right)+I_{k-1}\left(1-\exp\left(\frac{-\Delta t}{R_{\mathrm{df},k}C_{\mathrm{df},k}}\right)\right) \tag{31}$$

$$\frac{\partial g\left(U_{\mathrm{low},k}, I_k, \boldsymbol{\rho}_{\mathrm{low},k}\right)}{\partial C_{\mathrm{df}}}=\frac{\Delta t\left(U_{\mathrm{low},k}-R_{\mathrm{df},k}I_k\right)}{R_{\mathrm{df},k}\left(C_{\mathrm{df},k}\right)^2}\exp\left(\frac{-\Delta t}{R_{\mathrm{df},k}C_{\mathrm{df},k}}\right) \tag{32}$$

$$\frac{\partial g\left(U_{\mathrm{low},k}, I_k, \boldsymbol{\rho}_{\mathrm{low}}\right)}{\partial U_{\mathrm{low},k}}=\exp\left(\frac{-\Delta t}{R_{\mathrm{df},k}C_{\mathrm{df},k}}\right) \tag{33}$$

$$\frac{\mathrm{d}U_{\mathrm{low},k}}{\mathrm{d}\boldsymbol{\rho}_{\mathrm{low}}}=\frac{\partial g\left(U_{\mathrm{low},k-1}, I_{k-1}, \boldsymbol{\rho}_{\mathrm{low}}\right)}{\partial \boldsymbol{\rho}_{\mathrm{low}}}+\frac{\partial g\left(U_{\mathrm{low},k-1}, I_{k-1}, \boldsymbol{\rho}_{\mathrm{low}}\right)}{\partial U_{\mathrm{low},k-1}}\frac{\mathrm{d}U_{\mathrm{low},k-1}}{\mathrm{d}\boldsymbol{\rho}_{\mathrm{low}}} \tag{34}$$

$$\frac{\partial g\left(U_{\mathrm{low},k-1}, I_{k-1}, \boldsymbol{\rho}_{\mathrm{low},k-1}\right)}{\partial \boldsymbol{\rho}_{\mathrm{low}}}=\left[\frac{\partial g\left(U_{\mathrm{low},k-1}, I_{k-1}, \boldsymbol{\rho}_{\mathrm{low},k-1}\right)}{\partial R_{\mathrm{df}}}\quad\frac{\partial g\left(U_{\mathrm{low},k-1}, I_{k-1}, \boldsymbol{\rho}_{\mathrm{low},k-1}\right)}{\partial C_{\mathrm{df}}}\right] \tag{35}$$

$$\frac{\partial h\left(U_{\mathrm{low},k-1}, I_{k-1}, \boldsymbol{\rho}_{\mathrm{low},k-1}\right)}{\partial R_{\mathrm{df}}}=\frac{\Delta t\left(U_{\mathrm{low},k-1}-R_{\mathrm{df},k-1}I_{k-1}\right)}{C_{\mathrm{df},k-1}\left(R_{\mathrm{df},k-1}\right)^2}\exp\left(\frac{-\Delta t}{R_{\mathrm{df},k-1}C_{\mathrm{df},k-1}}\right)+I_{k-1}\left(1-\exp\left(\frac{-\Delta t}{R_{\mathrm{df},k-1}C_{\mathrm{df},k-1}}\right)\right) \tag{36}$$

$$\frac{\partial g\left(U_{\mathrm{low},k-1}, I_{k-1}, \boldsymbol{\rho}_{\mathrm{low},k-1}\right)}{\partial C_{\mathrm{df}}}=\frac{\Delta t\left(U_{\mathrm{low},k-1}-R_{\mathrm{df},k-1}I_{k-1}\right)}{R_{\mathrm{df},k-1}\left(C_{\mathrm{df},k-1}\right)^2}\exp\left(\frac{-\Delta t}{R_{\mathrm{df},k-1}C_{\mathrm{df},k-1}}\right) \tag{37}$$

$$\frac{\partial g\left(U_{\mathrm{low},k-1}, I_{k-1}, \boldsymbol{\rho}_{\mathrm{low},k-1}\right)}{\partial U_{\mathrm{low},k-1}}=\exp\left(\frac{-\Delta t}{R_{\mathrm{df},k-1}C_{\mathrm{df},k-1}}\right) \tag{38}$$

Comparing Eq. (29) with Eq. (34), it is not difficult to find that the calculation of the system output matrix $C_{\mathrm{low},k}^{\rho}$ is realized by the recursion of $\mathrm{d}U_{\mathrm{slow},k}/\mathrm{d}\boldsymbol{\rho}_{\mathrm{slow}}$. Specifically, when the state variables $\boldsymbol{\rho}_{\mathrm{slow},k-1}$ and $\mathrm{d}U_{\mathrm{slow},k-1}/\mathrm{d}\boldsymbol{\rho}_{\mathrm{slow}}$ slow are initialized, the results of $\mathrm{d}U_{\mathrm{slow},k}/\mathrm{d}\boldsymbol{\rho}_{\mathrm{slow}}$ slow can be calculated using Eqs. (34)–(38). Then, the calculation of $C_{\mathrm{low},k}^{\rho}$ is realized using Eqs. (29)–(33). Finally, the sub-algorithm designed based on EKF is applied in the low-frequency filter module. Then, the independent identification of low-frequency diffusion impedance parameters is completed iteratively. In this paper, we use a zero-mean matrix to initialize $\mathrm{d}U_{\mathrm{slow},k}/\mathrm{d}\boldsymbol{\rho}_{\mathrm{slow}}$. The specific iterative process of prediction and correction is as follows:

At the time $k=0$, Initialization:

$$\hat{\boldsymbol{\rho}}_{\mathrm{low},0}^{+}=E(\boldsymbol{\rho}_{\mathrm{low},0}) \tag{39}$$

$$\sum\nolimits_{\mathrm{low},0}^{+}=E[(\boldsymbol{\rho}_{\mathrm{low},0}-\hat{\boldsymbol{\rho}}_{\mathrm{low},0}^{+})(\boldsymbol{\rho}_{\mathrm{low},0}-\hat{\boldsymbol{\rho}}_{\mathrm{low},0}^{+})^{\mathrm{T}}] \tag{40}$$

At the time $k=1,2,...$, repeat:

$$\hat{\boldsymbol{\rho}}_{\mathrm{low},k}^{-}=\hat{\boldsymbol{\rho}}_{\mathrm{low},k-1}^{+} \tag{41}$$

$$\sum\nolimits_{\mathrm{low},k}^{-}=\sum\nolimits_{\mathrm{low},k-1}^{+}+\sum\nolimits_{w} \tag{42}$$

$$K_{\mathrm{low},k}^{\rho}=\sum\nolimits_{\mathrm{low},k}^{-}\left(\boldsymbol{C}_{\mathrm{low},k}^{\rho}\right)^{\mathrm{T}}\left(\boldsymbol{C}_{\mathrm{low},k}^{\rho}\sum\nolimits_{\mathrm{low},k}^{-}(\boldsymbol{C}_{\mathrm{low},k}^{\rho})^{\mathrm{T}}+\sum\nolimits_{v}\right)^{-1} \tag{43}$$

$$\hat{\boldsymbol{\rho}}_{\mathrm{low},k}^{+}=\hat{\boldsymbol{\rho}}_{\mathrm{low},k}^{-}+K_{\mathrm{low},k}^{\rho}\left(U_{\mathrm{df},m}-g\left(U_{\mathrm{low},k},I_{k},\hat{\boldsymbol{\rho}}_{\mathrm{low},k}^{-}\right)\right) \tag{44}$$

$$\sum\nolimits_{\mathrm{low},k}^{+}=\left(\boldsymbol{E}-K_{\mathrm{low},k}^{\rho}\boldsymbol{C}_{\mathrm{low},k}^{\rho}\right)\sum\nolimits_{\mathrm{low},k}^{-} \tag{45}$$

From Eqs. (39)–(45), $K_{\mathrm{low},k}^{\rho}$ and $\Sigma_{\mathrm{low},k}$ are the Kalman gain matrix and covariance matrix of the low-frequency sub-algorithm at the time step k, respectively. Σ_{w} and Σ_{v} are the covariance matrix of noise $\boldsymbol{w}_{k}$ and noise v_{k} respectively. In addition, similar to Eq. (24), $U_{\mathrm{df},m}$ is the identification result of U_{df} of the mth recursive under the medium-high frequency sub-algorithm. The Kalman gain matrix $K_{\mathrm{low},k}^{\rho}$ corrects the error innovation $\Sigma_{\mathrm{low},k}$ of the diffusion voltage in each iteration calculation so that

the identification results of the low-frequency state parameters R_{df} and C_{df} can be optimal. Moreover, the design of two independent filters, medium-high-frequency, and low-frequency will make the physical meaning of the model parameters more obvious. The entropy of the parameters is smaller in the whole identification framework.

3.2 Design of adaptive drive controller

In the development of an adaptive multi-time scale identification strategy, the medium-high frequency sub-algorithm based on FFRLS and the low-frequency sub-algorithm based on EKF are designed in different modules jointly but separately. For the medium-high frequency filter module, it is appropriate to use the measured voltage and current data sampled by the ECU. However, for the low-frequency filter module, as described above, the large diffusion time constant makes the measurement data such as voltage and current unable to be directly applied. Driven by this kinetic response, a crucial problem is determining the driving mode of the medium-high frequency sub-algorithm.

A natural solution is a design of a fixed driving time, which is the same as the idea described in Ref. [39]. However, under the real driving conditions of EVs with drastic current changes, the fixed driving time brings some ineffective innovations to the identification of diffusion impedance links. Especially under the mixed charging-discharging condition, the identification efficiency of the low-frequency algorithm is greatly reduced. An extreme but typical example is that under the condition of charge-discharge at the same rate, the current of charging and discharging at the same time causes the diffusion impedance voltage changes to cancel each other out. Therefore, it is crucial and necessary to design an adaptive drive controller to ensure the start and stop of the low-frequency sub-algorithm.

Considering that the terminal voltage change of the diffusion impedance link is determined by the current on the diffusion capacitor, the same current profile will pass through the OCV link of the battery

while flowing through the diffusion capacitor. The change in open circuit voltage is strongly related to the change in battery SOC. With this analysis, an effective adaptive drive controller is designed based on the variation of SOC so that the whole parameter identification algorithm can adapt to all current profiles. Based on Eq. (4), the change in SOC under laboratory conditions can be calculated using Eq. (46).

$$\Delta z = \Delta t \cdot \eta_I \sum_{i=1}^{n} I_i / C_{\text{nom}} \tag{46}$$

where Δz represents the change in SOC level, and n represents the total number of sampling times required when the SOC variation reaches the preset value of Δz. In this paper, we set Δz to 0.5% based on the OCV-SOC curve of the selected battery samples. This means that when the change in SOC reaches 0.5%, the same current profile will bring a more obvious diffusion voltage change so that the low-frequency sub-algorithm can get relevant information for iterative calculation.

3.3 Overall framework of the proposed strategy

From the above-detailed description, the adaptive multi-time scale identification strategy for second-order RC ECM parameters is developed, which mainly includes the sub-algorithm design in the medium-high frequency filter module, the sub-algorithm design in the low-frequency filter module, the determination of coupling factors among different modules, and the design of an adaptive drive controller. Besides ensuring the accuracy of macro-characteristic descriptions, the most important contribution of this strategy is to greatly reduce the entropy of key kinetic characteristic identification results. Fig. 2 shows the overall iterative framework of the adaptive multi-time scale identification strategy considering variable characteristic frequency for the second-order RC ECM.

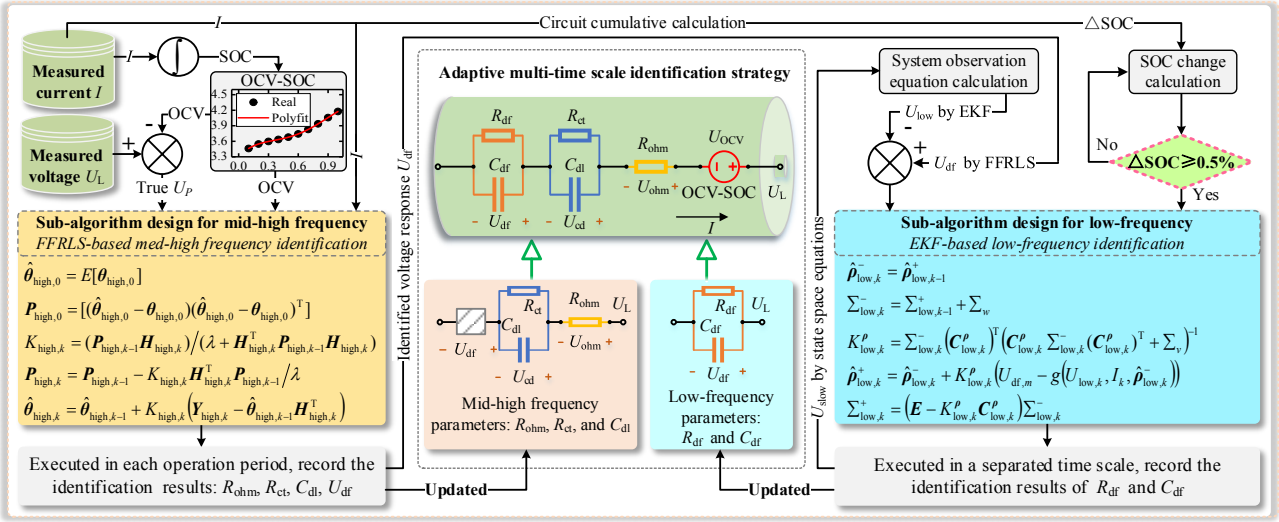

Fig. 2. Overall framework of the adaptive multi-time scale identification strategy.

The development of the adaptive multi-time scale identification strategy aims to improve the capture ability of key feature parameters in battery modeling, which makes the identification results of model parameters have obvious physical significance. It can be observed from the iterative framework shown in Fig. 2 that the two sub-algorithms run in their respective frequency bands and are coupled by diffusion voltage. There are two points worth explaining, as follows:

First, it can be observed that the realization of the two sub-algorithms depends on the SOC value of the battery. In this paper, we simplify the calculation of battery SOC based on the Coulomb counting method. In addition, the OCV-SOC curve is acquired in a completely balanced battery state. Also, the current is sampled using a high-precision battery tester in the laboratory. Therefore, it is believed that the initial value of battery SOC and the calculated value during the experiment have acceptable accuracy. Second, special consideration is given to the algorithm's computational complexity to achieve the online identification efficiency of model parameters in BMS mounted on EVs. It can be observed from Fig. 2 that the RC ECM-based implementation for modeling the key kinetic physical processes inside the battery and the development of an adaptive multi-time scale identification strategy do not introduce new unknown variable parameters. Therefore, the whole modeling strategy does not impose an additional

computational burden on the embedded application of the system. In fact, due to the unique design of the driving mode, the parameters of the low-frequency impedance link are identified only at a specific time, which greatly reduces the computational complexity of the whole strategy compared with the traditional fixed characteristic frequency identification method.

4 Experimental validation and discussions

4.1 Experimental platform and configurations

In the verification phase of the algorithm, the NCM battery samples with a capacity of 2.0 A h are selected. Furthermore, the experiments of three different current profiles, including the federal urban driving schedule (FUDS), Beijing dynamic stress test (BJDST), and urban dynamometer driving schedule (UDDS), are designed and conducted. The experiment platform is built with a high-precision battery test system, temperature chamber, and host computer for recording experimental data. The main characteristic parameters of the cell and the power line connection of each device in the experimental platform are shown in Fig. 3.

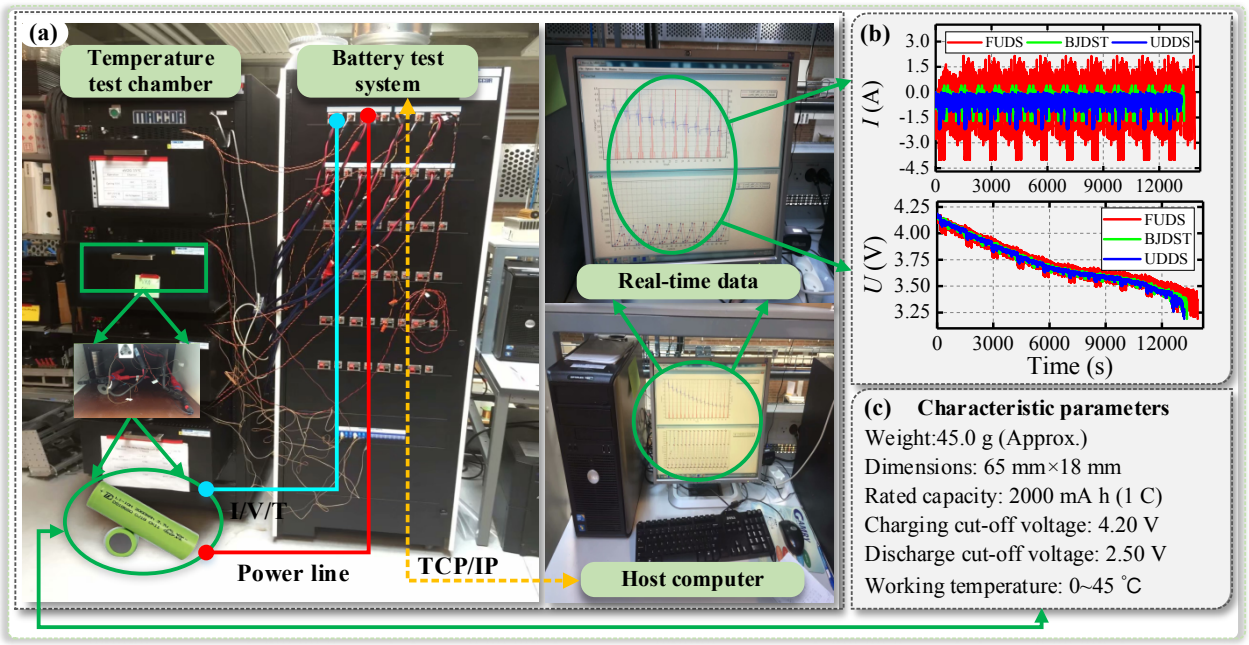

Fig. 3. Experimental platform and configurations. (a) Experimental platform; (b) current profile and voltage response; (c) battery characteristic parameters.

It is worth noting that, influenced by many factors, such as temperature and aging state, the model parameters inside the battery are time-varying. To control the influence of these parameters as much as possible, the same battery sample is placed in a temperature-controlled box set at 25 °C in advance. Before the FUDS, BJDST, and UDDS experiments, the batteries in the temperature-controlled box are put on hold for a long enough time to achieve the internal state balance, thus reducing the influence of temperature and aging on the experimental results. Under this consideration and setting, the experimental data for three working conditions are shown in Fig. 4.

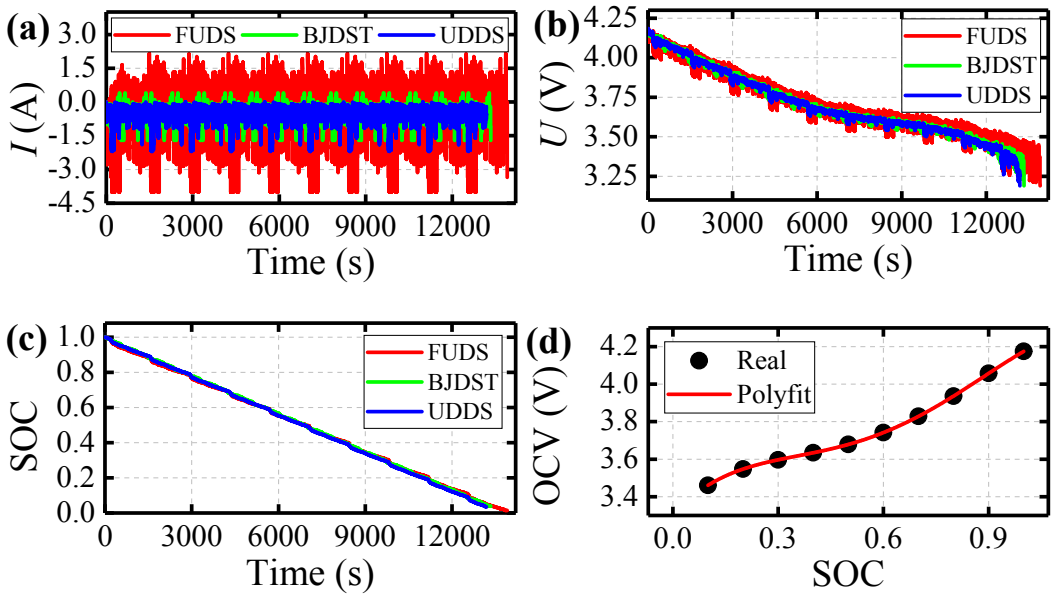

Fig. 4. Experimental results under different working conditions. (a) Current profile; (b) coltage response; (c) SOC curve; (d) OCV-SOC fitting results.

Fig. 4(a)–(c) show the measured current, measured voltage, and SOC calculation curves of FUDS, BJDST, and UDDS experiments in the laboratory environment. Fig. 4(d) shows the OCV test data of the battery and the fitting results of the OCV-SOC. It is worth noting that high-order fitting may improve the calculation accuracy for known data points. However, it is also easy to reduce the calculation accuracy for OCV of unknown points, which increases the computational complexity. Because this paper

aims to solve the problem of high-accuracy identification of the model parameters, the hysteresis effect of OCV is not considered, and the functional relationship of OCV-SOC is realized by conventional fourth-order fitting. As mentioned above, every value of OCV is sampled by a high-precision battery test system when the battery is fully laid aside to achieve complete balance. Therefore, based on the fitting relationship between the OCV and SOC, an accurate initial SOC value is obtained.

4.2 Accuracy verification of voltage prediction

Based on the above discussion, FUDS, BJDST, and UDDS experiments are tested on battery samples. The development of the adaptive identification strategy proposed in this paper is realized by coupling the medium-high frequency sub-algorithm based on the FFRLS algorithm and the low-frequency sub-algorithm based on the EKF algorithm. Therefore, the FFRLS algorithm and the EKF algorithm are selected at the fixed characteristic frequency to compare the performance of the proposed strategy. First of all, the terminal voltage tracking effect of the model is verified by comparison, and the experimental results are shown in Fig. 5.

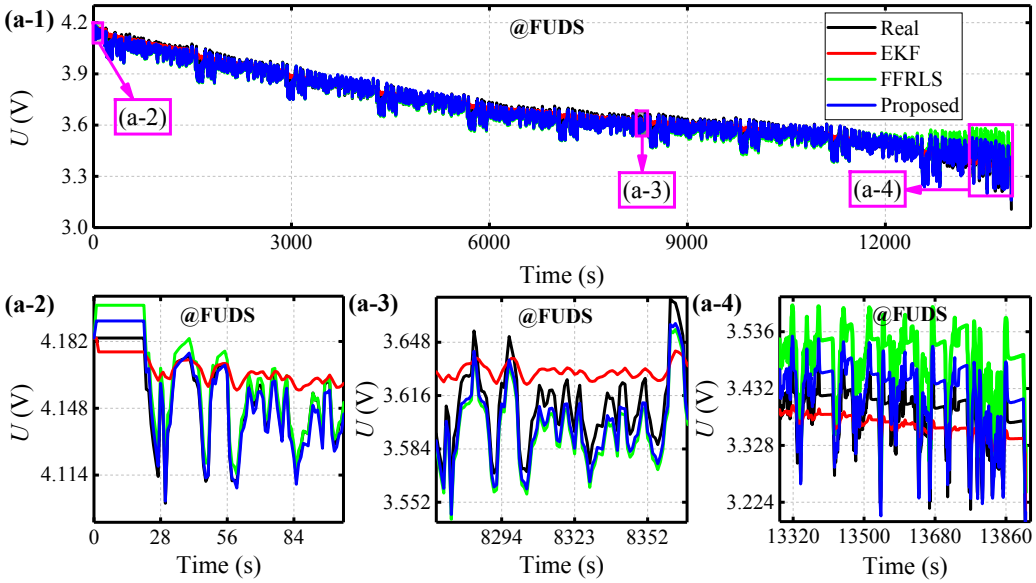

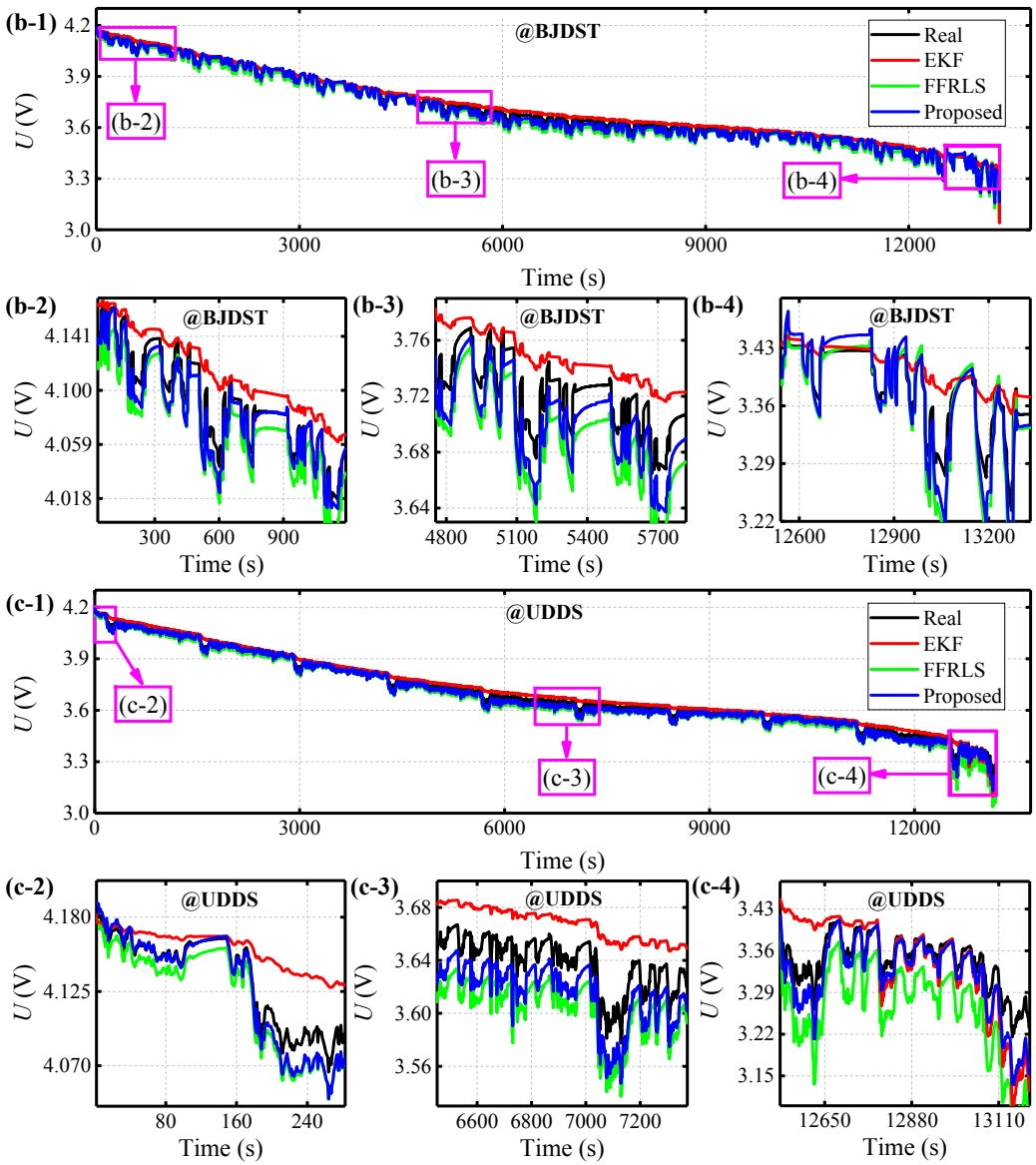

Fig. 5. Tracking effects of terminal voltage under different working conditions. (a–1) FUDS; (a–2, a–3, a–4) partial profiles of FUDS; (b–1) BJDST; (b–2, b–3, b–4) partial profiles of BJDST; (c–1) UDDS; (c–2, c–3, c–4) partial profiles of UDDS.

It can be observed from Fig. 5 that the EKF algorithm, the FFRLS algorithm, and the proposed strategy can track the terminal voltage of the model in the trend. From the tracking effect, compared with the EKF algorithm, the FFRLS algorithm and the proposed strategy perform better at matching ohmic resistance characteristics. However, the characterization of the FFRLS algorithm in terms of the medium-high-frequency charge transfer effect and the low-frequency diffusion effect is insufficient. By comparison, the proposed strategy can match well whether it is ohmic resistance or charge transfer and

diffusion characteristics of carriers. One of the main reasons is that the characteristics of the frequency difference of the complex dynamics inside the battery are considered. Furthermore, the terminal voltage error results under three working conditions are shown in Fig. 6.

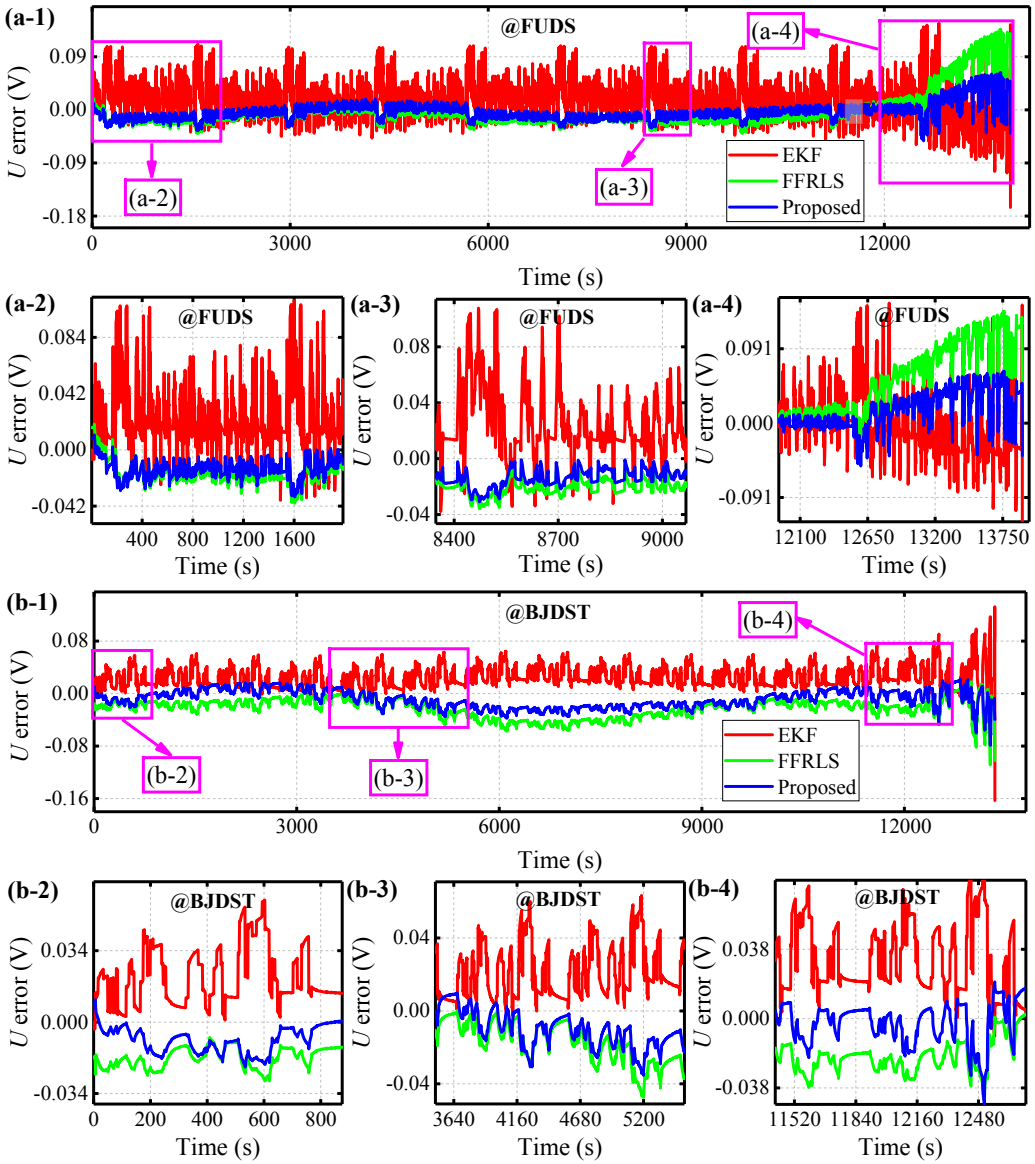

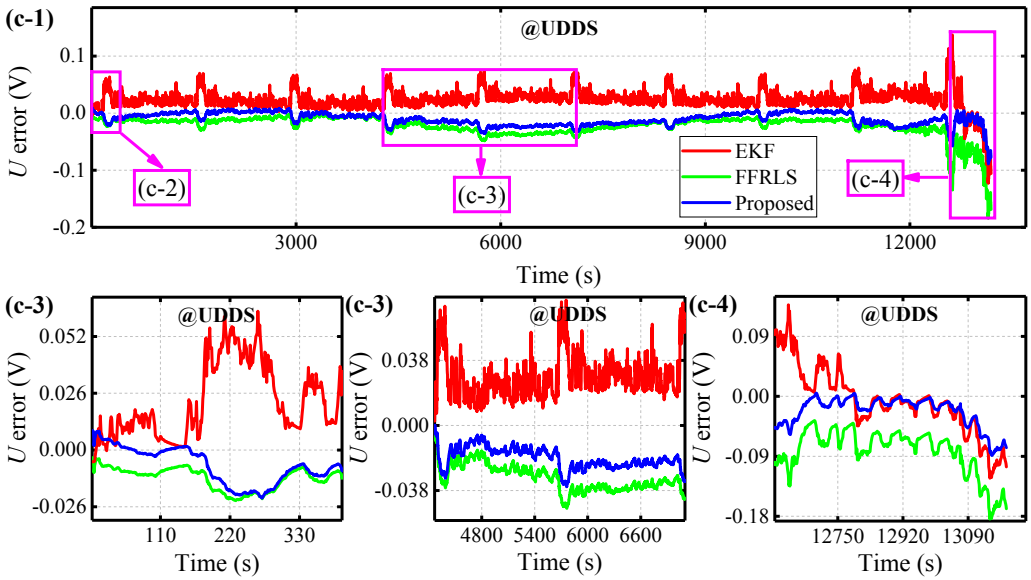

Fig. 6. Estimation error of terminal voltage under different working conditions. (a–1) FUDS; (a–2, a–3, a–4) partial profiles of FUDS; (b–1) BJDST; (b–2, b–3, b–4) partial profiles of BJDST; (c–1) UDDS; (c–2, c–3, c–4) partial profiles of UDDS.

From the error result curve shown in Fig. 6, the superiority of the proposed strategy in predicting the terminal voltage can be clearly observed. Under three different current profiles, the error result of the proposed strategy is always smaller than that of the traditional fixed characteristic frequency identification method, especially at the later stage of discharge. Two reasons lead to the above results. Firstly, the influence of model parameters. The proposed strategy distinguishes the complex kinetic processes inside the battery, which makes the modeling of the key internal kinetic processes more accurate, especially in the low-frequency diffusion impedance link. Secondly, the influence of working conditions. Because the trend of the whole working condition is continuous discharge, the function of the low-frequency sub-algorithm is fully stimulated by the accumulation of current. Additionally, this means that as the discharge process continues, it will become increasingly clear how the diffusion response of carriers within the battery affects solid particles. In addition, because the low-frequency sub-algorithm and the medium-high frequency sub-algorithm are closed-loop coupled through the diffusion voltage, the stability performance of the proposed strategy is better than that of the traditional fixed

characteristic frequency FFRLS and EKF algorithms. Furthermore, the performance of the model is quantitatively analyzed using the mean absolute error (MAE) and root-mean-square error (RMSE) metrics. Their corresponding mathematical expressions can be found in Refs. [14,24]. The voltage modeling results based on different methods under different working conditions are shown in Table 1.

Table 1. MAE and RMSE of voltage modeling based on different methods.

	FUDS		BJDST		UDDS	
	MAE (mV)	RMSE (mV)	MAE (mV)	RMSE (mV)	MAE (mV)	RMSE (mV)
EKF	22.95	30.72	25.78	30.51	24.88	28.74
FFRLS	19.57	29.82	22.86	26.56	22.13	28.73
Proposed	11.19	14.79	12.93	15.78	11.46	15.16

It can be observed from Table 1 that MAE and RMSE under the proposed strategy are lower than those of traditional fixed characteristic frequency EKF and FFRLS identification methods under the three working conditions. Compared with FFRLS and EKF, under the FUDS condition, the MAE of the proposed strategy is reduced by 11.76 and 8.38 mV, and the RMSE is reduced by 15.93 and 15.03 mV, respectively. Under the BJDST condition, the MAE of the proposed strategy is reduced by 12.85 and 9.93 mV, and the RMSE is reduced by 14.73 and 10.78 mV, respectively. Under the UDDS condition, the MAE of the proposed strategy is reduced by 13.42 and 10.67 mV, and the RMSE is reduced by 13.58 and 13.57 mV, respectively. Compared with Ref. [41] (based on the least squares algorithm at a single time scale, the RMSE of the end-voltage prediction results at 25 °C is 37.20 mV), the proposed algorithm improves the RMSE of terminal voltage prediction at three operating conditions by 22.41, 21.42, and 22.04 mV, respectively. The above experimental results can prove that the proposed algorithm has excellent performance and high accuracy in battery terminal voltage prediction.

4.3 Model-based parameters identification results

Under the verification of the above terminal voltage performance, the parameter capture results under different working conditions are recorded to verify the characterization performance of the model in key characteristic parameters. The proposed identification strategy considers the variable characteristic frequency inside the battery and divides the impedance links in different frequency bands into different filter modules. Under three different test data sets, the sub-algorithm in the medium-high frequency filter runs under each sample data. Then, the results of the medium-high frequency impedance characteristic parameters R_{ohm}, R_{ct}, and C_{dl} under the full sequence are obtained, as shown in Fig. 7.

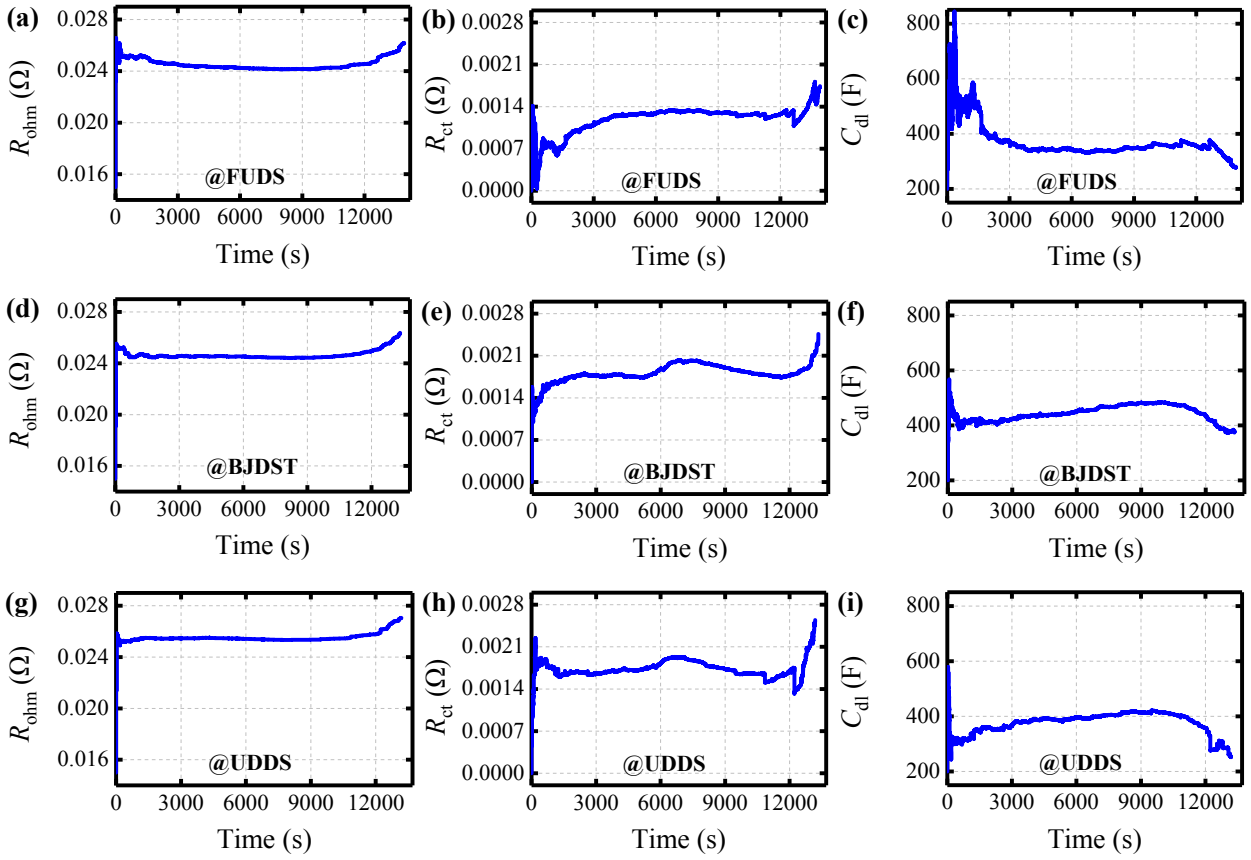

Fig. 7. Identification results of medium-high frequency parameters under different working conditions. (a–c) FUDS; (d–f) BJDST; (g–i) UDDS.

By observing Fig. 7, it can be observed that all medium-high frequency impedance parameters converge rapidly under different working conditions based on the proposed method. In addition, it is

observed from the convergence values of the identification results that the maximum error of the R_{ohm} does not exceed 1.08 mΩ, the maximum error of the R_{ct} does not exceed 0.60 mΩ, and the maximum error of the C_{dl} does not exceed 0.09 kF under different operating conditions. It is verified that the identification results of each parameter based on the proposed multi-time scale identification strategy have high consistency and strong stability. The main reason for this phenomenon is that the medium-high frequency sub-algorithm actively isolates the influence of the low-frequency reaction process inside the battery. While the medium-high frequency sub-algorithm iterates, the low-frequency sub-algorithm based on EKF is controlled to run at a specific time to identify the results of the diffusion impedance characteristic parameters R_{df} and C_{df}, as shown in Fig. 8.

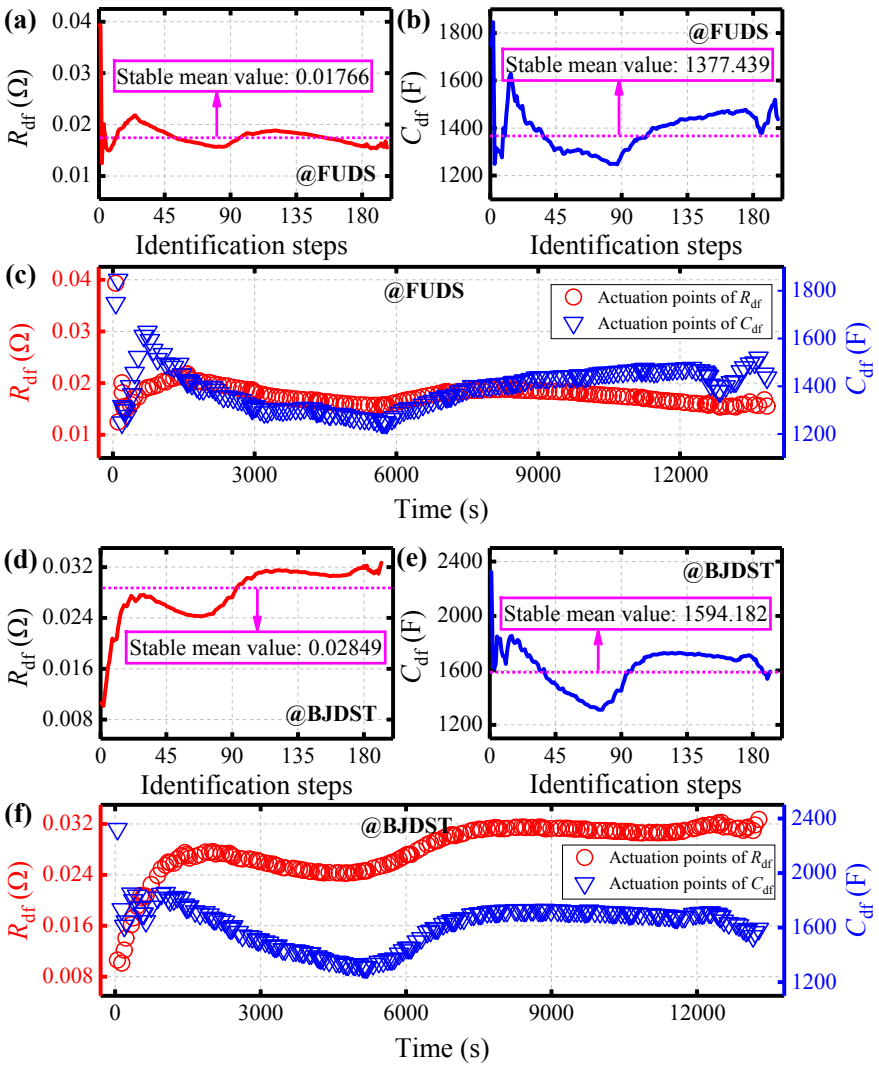

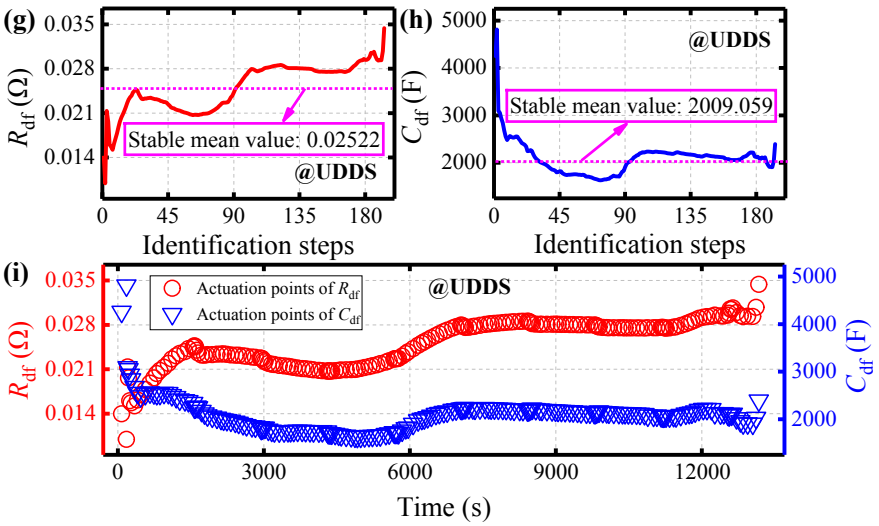

Fig. 8. Identification results of low-frequency parameters under different working conditions. (a, b) FUDS; (d, e) BJDST; (g, h) UDDS; (c, f, i) results of driving points of low-frequency sub-algorithm.

Fig. 8(a, d, and f) respectively show the parameter changes of diffusion resistance. Fig. 8(b, e, and h) respectively show the identification results of diffusion capacitance parameters. The Fig. 8(c, f, and i) respectively show the driving points of the low-frequency sub-algorithm in full sequence under different working conditions. Compared with Fig. 7, an obvious difference can be noticed, that is, the abscissa of the parameter curve in Fig. 8(a, d, and f) and Fig. 8(b, e, and h) is not the traditional time but the identification step. This is because the design of the adaptive drive controller makes the low-frequency sub-algorithm only execute on a specific time scale. It can be observed from Fig. 8(c, f, and i) that the proposed model has at least three obvious advantages. Firstly, the influence of the characteristics of medium-high-frequency parameters on the identification of low-frequency parameters is reduced. Secondly, the algorithm's unnecessary iterations and the computational load of the system are greatly reduced. Finally, the proposed strategy can adapt to different current profiles and improve its generalization ability.

4.4 Reliability analysis of the model parameters

For the battery model with superior performance, besides its excellent voltage prediction ability,

the capture of key characteristic parameters should also be given attention. Based on this core, the statistical analysis of the parameter identification results under various working conditions and the extraction of the parameter features that lead to the stable phase of the algorithm are performed. Then, the normalized values are calculated by normalizing the identification results under BJDST and UDDS with the results of FUDS as a scale. In addition, the entropy value calculation of the model parameters is proposed and applied for the first time in this paper. Its calculation method is described in detail in Section 2. It is worth noting that since the entropy value is defined by a percentage, the average value is coupled with at least two kinds of working condition data. Therefore, it is reasonable to compare the parameters of resistance and capacitance with different dimensions. The normalization and entropy calculation results for the parameters are shown in Fig. 9.

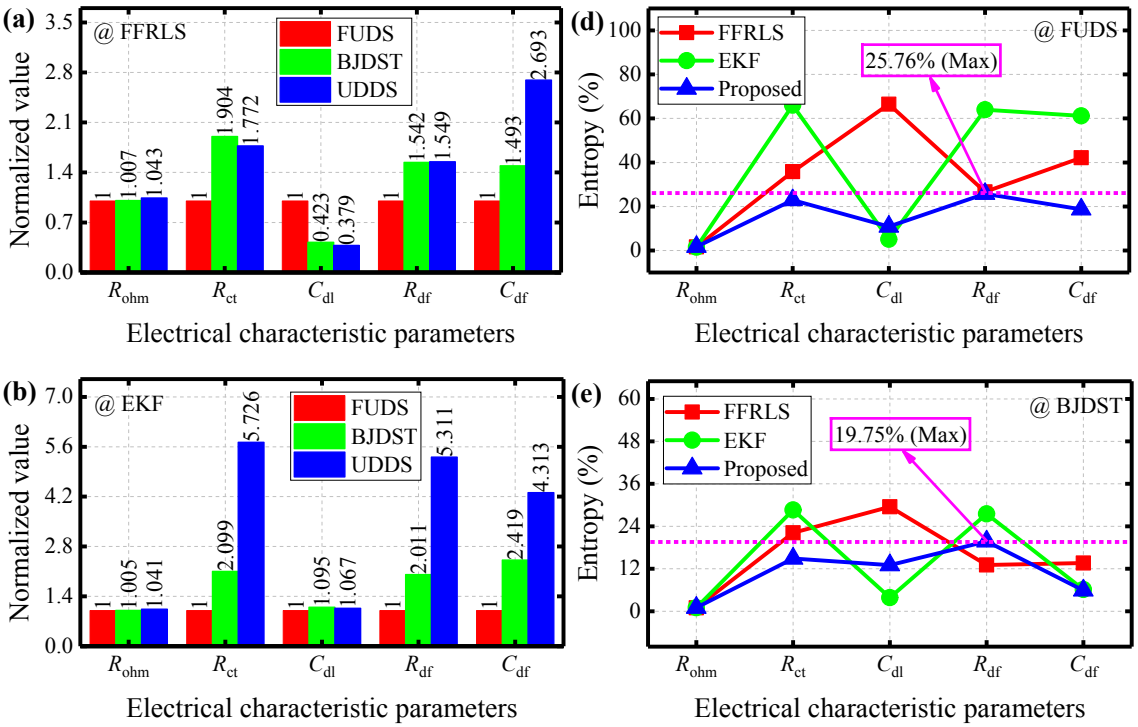

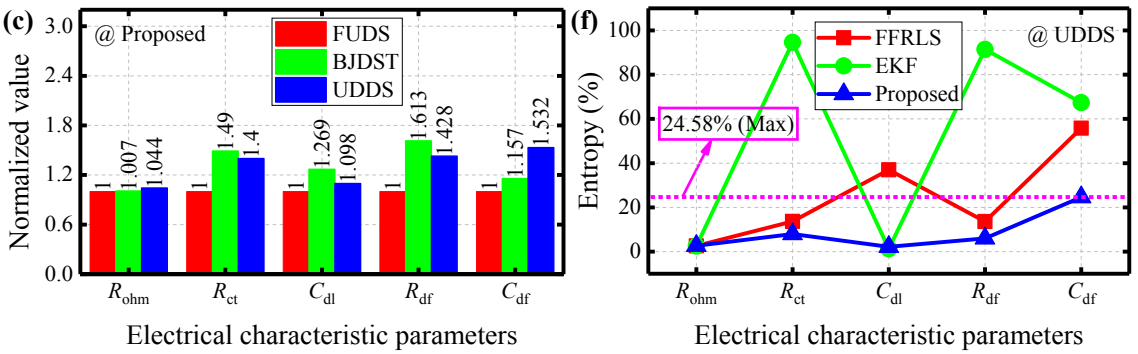

Fig. 9. Reliability verification results of model parameter identification. (a–c) Normalized value under different working conditions; (d–f) entropy based on parameters under different algorithms.

From the results shown in Fig. 9(a–c), it can be observed that the parameters identified using the FFRLS and EKF algorithms are highly inconsistent under different working conditions. Meanwhile, the model parameters captured by the proposed algorithm from different working conditions are consistent. This shows that the parameter results based on the proposed algorithm have more explicit physical significance. In addition, the entropy value is another angle to analyze the rationality and reliability of the algorithm identification results, that is, the dispersion of parameter identification results based on different algorithms under the same working condition. It can be observed from the results shown in Fig. 9(d–f) that under the FUDS, BJDST, and UDDS working conditions, the maximum entropy values of recognition results based on the FFRLS algorithm are 66.49%, 21.17%, and 55.79%, respectively. The maximum entropy values of the recognition results based on the EKF algorithm are 66.01%, 28.63%, and 94.64%, respectively. The maximum entropy values of recognition results based on the proposed strategy are 25.76%, 19.75%, and 24.58%, respectively. Compared with the FFRLS-based model identification results, the proposed strategy reduces the parameter dispersion by 40.72%, 2.41%, and 31.20%, respectively. Compared with the EKF-based model identification results, the proposed strategy reduces the parameter dispersion by 40.25%, 8.88%, and 70.05%, respectively. This fully demonstrates that the model parameter identification results based on the proposed strategy are more accurate and

reliable.

5 Conclusions

In this paper, the impact of multi-time scale effects of key kinetic processes on the battery modeling is investigated. An efficient adaptive multi-time scale identification strategy that takes into account the frequency difference property is proposed in detail. Compared with the battery modeling strategy at a single time scale, the four main conclusions of this paper are as follows.

(1) Different kinetic processes within the cell exhibit specific relaxation times. The second-order ECM that takes into account timescale information enables the modeling of key kinetic processes without adding additional computational complexity.

(2) An adaptive multi-time scale identification strategy is extracted and implemented based on the variable characteristic frequency for the key kinetic processes. The proposed modeling strategy couples the key dynamical processes at high frequency, medium-high frequency, and low frequency by decoupling them using the corresponding time scale information.

(3) The coupled iterative calculation of the two sub-filter modules at different time scales is achieved based on the voltage response of the diffusion process. In addition, the adaptive identification of low-frequency dynamics parameters is achieved using a driver design based on the level of SOC variation.

(4) The concept of entropy is introduced and advocated to verify the physical meaning of kinetic parameters. The entropy calculation is implemented using the parameter identification data under different working conditions and algorithms to verify the superiority of the proposed method in the identification of key kinetic parameters.

Experimental results under three different working conditions show that, from the perspective of

modeling voltage, the MAE and RMSE of the voltage tracking based on the proposed strategy are limited to 13 and 16 mV, respectively. Meanwhile, compared with the FFRLS and EKF algorithms at the fixed characteristic frequency, the maximum reduction values of the MAE index under the three working conditions are 13.34 and 10.67 mV, respectively. The maximum reduction values of the RMSE index are 15.94 and 15.04 mV, respectively. From the perspective of model parameters, compared with the fixed characteristic frequency identification algorithm based on FFRLS and EKF, the proposed strategy reduces the maximum entropy of model parameters by 40.72% and 70.05%, respectively. The proposed multi-time scale modeling method can provide a sufficient theoretical basis for the subsequent development and embedded application of a high-performance adaptive state estimator based on ECM.

Acknowledgments

This work was supported by the National Natural Science Foundation of China (Grant No. 62173281, 51975319, and 61801407) and the State Key Laboratory of Tribology and Institute of Manufacturing Engineering at Tsinghua University. To our co-author, Prof. Carlos Fernandez of Robert Gordon University, we appreciate your support. The authors would also like to thank Prof. D.-I. Stroe at Aalborg University for reviewing & editing.

References

[1] H. Pang, L. Wu, J. Liu, X. Liu, K. Liu, J. Energy Chem. 78 (2022) 1–12.

[2] J. Tian, R. Xiong, J. Lu, C. Chen, W. Shen, Energy Storage Mater. 50 (2022) 718–729.

[3] H. You, J. Zhu, X. Wang, B. Jiang, H. Sun, X. Liu, X. Wei, G. Han, S. Ding, H. Yu, W. Li, D.U. Sauer, H. Dai, J. Energy Chem. 72 (2022) 333–341.

[4] Y. Wang, X. Zhang, Z. Chen, Appl. Energy 313 (2022) 118832.

[5] X. Sun, M. Ouyang, H. Hao, Joule 6 (2022) 1738–1742.

[6] M. Contestabile, G.J. Offer, R. Slade, M. Thoennes, Energy Environ. Sci. 4 (2011) 3754–3772.

[7] Y. Zheng, M. Ouyang, X. Han, L. Lu, J. Li, J. Power Sources 377 (2018) 161–188.

[8] S. Yuan, C. Chang, S. Yan, P. Zhou, X. Qian, M. Yuan, K. Liu, J. Energy Chem. 62 (2021) 262–280.

[9] B. Su, S. Wu, H. Liang, Q. Gu, H. Wang, W. Zhou, X. Zhao, T. Zhang, P.H.L. Sit, W. Zhang, D.Y.W. Yu, J. Power Sources 517 (2022) 230728.

[10] J. Tian, R. Xu, Y. Wang, Z. Chen, Energy 221 (2021) 119682.

[11] Y. Li, X. Gao, X. Feng, X. Han, J. Du, L. Lu, M. Ouyang, J. Energy Chem. 67 (2022) 34–45.

[12] H. Dai, T. Xu, L. Zhu, X. Wei, Z. Sun, Appl. Energy 184 (2016) 119–131.

[13] R. Xiong, J. Tian, W. Shen, J. Lu, F. Sun, J. Energy Chem. 76 (2023) 404–413.

[14] K. Luo, X. Chen, H. Zheng, Z. Shi, J. Energy Chem. 74 (2022) 159–173.

[15] Y. Che, Y. Zheng, Y. Wu, X. Sui, P. Bharadwaj, D.I. Stroe, Y. Yang, X. Hu, R. Teodorescu, Appl. Energy 323 (2022) 119663.

[16] F. Sun, R. Xiong, H. He, W. Li, J.E.E. Aussems, Appl. Energy 96 (2012) 378–386.

[17] K. Liu, C. Zou, K. Li, T. Wik, IEEE Trans. Ind. Informatics 14 (2018) 5463–5474.

[18] L. Wu, K. Liu, H. Pang, Electrochim. Acta 368 (2021) 137604.

[19] X. Feng, M. Ouyang, X. Liu, L. Lu, Y. Xia, X. He, Energy Storage Mater. 10 (2018) 246–267.

[20] X. Hu, L. Xu, X. Lin, M. Pecht, Joule 4 (2020) 310–346.

[21] L. Liu, X. Feng, C. Rahe, W. Li, L. Lu, X. He, D.U. Sauer, M. Ouyang, J. Energy Chem. 61 (2021) 269–280.

[22] X. Hu, X. Deng, F. Wang, Z. Deng, X. Lin, R. Teodorescu, M.G. Pecht, Proc. IEEE 110 (2022) 735–753.

[23] L. Liu, B. Xu, Z. Yan, W. Zhou, Y. Li, R. Mai, Z. He, IEEE Trans. Power Electron. 36 (2020) 4931–4936.

[24] J. Tian, R. Xiong, W. Shen, F. Sun, Energy Storage Mater. 37 (2021) 283–295.

[25] J. Tian, X. Liu, C. Chen, G. Xiao, Y. Wang, Y. Kang, P. Wang, IEEE Trans. Intell. Transp. Syst. 24 (2023) 446–458

[26] L. Liu, R. Mai, B. Xu, W. Sun, W. Zhou, Z. He, IEEE Trans. Power Electron. 36 (2021) 9160–9169.

[27] Y. Che, Z. Deng, X. Lin, L. Hu, X. Hu, IEEE Trans. Veh. Technol. 70 (2021) 1269–1277.

[28] J. Tian, R. Xiong, W. Shen, J. Lu, X.G. Yang, Joule 5 (2021) 1521–1534.

[29] D. Capkova, V. Knap, A.S. Fedorkova, D.I. Stroe, J. Energy Chem. 72 (2022) 318–325.

[30] S.M.M. Alavi, C.R. Birkl, D.A. Howey, J. Power Sources 288 (2015) 345–352.

[31] Y. Lu, C. Zhao, J. Huang, Q. Zhang, Joule 6 (2022) 1172–1198.

[32] F. Guo, G. Hu, S. Xiang, P. Zhou, R. Hong, N. Xiong, Energy 178 (2019) 79–88.

[33] Z. Yang, X. Wang, J. Energy Storage 59 (2023) 106462.

[34] E. Samadani, S. Farhad, W. Scott, M. Mastali, L.E. Gimenez, M. Fowler, R.A. Fraser, Electrochim. Acta 160

(2015) 169–177.

[35] N. Devillers, M.C. Péra, S. Jemei, F. Gustin, D. Bienaimé, Int. J. Electr. Power Energy Syst. 67 (2015) 168–178.

[36] Y. Duan, J. Tian, J. Lu, C. Wang, W. Shen, R Xiong, Energy Storage Mater. 41 (2021) 24–31.

[37] H. Shi, S. Wang, L. Wang, W. Xu, C. Fernandez, B.E. Dablu, Y. Zhang, J. Power Sources 517 (2022) 230725.

[38] B. Xu, Z. Yan, L. Xiong, L. Zhang, W. Zhou, R. Mai, Z. He, IEEE Trans. Ind. Electron. 70 (2022) 2596–2606.

[39] J. Tian, R. Xiong, W. Shen, J. Lu, Appl. Energy 291 (2021) 116812.

[40] H. Shi, S. Wang, C. Fernandez, C. Yu, Y. Fan, W. Cao, Int. J. Energy Res. 45 (2021) 15323–15337.

[41] Y. Wang, C. Zhou, Z. Chen, Energy 241 (2022) 122877.

[42] Y. Hu, Y. Wang, IEEE Trans. Control Syst. Technol. 23 (2014) 1180–1188.

[43] C. Jiang, S. Wang, B. Wu, C. Fernandez, X. Xiong, J. Coffie-Ken, Energy 219 (2021) 119603.

[44] H. Shi, S. Wang, C. Fernandez, C. Yu, W. Xu, B.E. Dablu, L. Wang, Appl. Energy 324 (2022) 119789.

[45] Y. Wang, Z. Chen, Appl. Energy 260 (2020) 114324.

[46] T.G. Voskuilen, H.K. Moffat, B.B. Schroeder, S.A. Roberts, J. Power Sources 488 (2021) 229469.

[47] H. Shi, L. Wang, S. Wang, C. Fernandez, X. Xiong, B.E. Dablu, W. Xu, J. Energy Storage 50 (2022) 104309.

[48] A. Wehrl, Rev. Mod. Phys. 50 (1978) 221.

[49] A. Rényi, Proc. Fourth Berkeley Symp. Math. Stat. Probab. 1 (1961) 547–561.

[50] L. Jost, Oikos 113 (2006) 363-375.

[51] Z. Khalik, M.C.F. Donkers, H.J. Bergveld, J. Power Sources 488 (2021) 229427.

[52] J. Peng, H. Shi, S. Wang, L. Wang, C. Fernandez, X. Xiong, B.E. Dablu, Energy Sci. Eng. 10 (2022) 3727–3740.